Characterizing Grain Boundary Network Length Features through a Harmonic Representation

Christopher W. Adair[a,*], Oliver K.Johnson[a]

[a]*Department of Mechanical Engineering, Brigham Young University, Provo, UT 84602, USA*

Abstract

When modeling and characterizing grain boundary networks (GBNs), there are situations where local descriptors such as triple junction fractions (TJFs) and special boundary fractions are identical between two microstructures, but the performance or properties between the two are distinct. These differences are caused by higher length-scale features that cannot be identified using local structural descriptors. Spectral graph theory (SGT) has been used previously to encode network length features, but did not enable direct quantitative comparisons between the structures that cause property differences. In this paper, we derive a harmonic representation of diffusion on GBNs based on SGT. This method enables direct quantitative comparisons between GBNs for microstructures with different morphologies, and identifies network length features responsible for structural and performance differences, which local descriptors cannot explain. We show an interpretation of the eigenmodes generated by this method that explains long-range structural causes of certain property differences. We apply this method to a large library of microstructures, and identify structural classes through clustering. We show that equal proportioned TJF and J_1 dominated microstructures are the most sensitive to network length differences because of boundary configurations, while J_2-J_3 dominated structures are the least sensitive. This method also identifies network length features that result in anomalous percolation/non-percolation compared to predictions based on local correlations alone.

Keywords: Grain Boundary, Grain Boundary Networks, Spectral Graph Theory

---

1. Introduction

In microstructural materials characterization, the grain boundary network (GBN) is a high-dimensional feature that describes the connectivity of grain boundaries [1]. As multiple macroscopic properties are dependent on the configuration and properties of grain boundaries, interpreting the structure of the GBN is important to undertanding the behavior of micro to macro structure-property models [1–5].

Due to the high-dimensional nature of GBNs, quantitatively describing the similarities and differences between them presents a challenge. Statistical measures such as triple junction fractions (TJFs) are useful as long as the property of interest does not depend on connectivity further than a single triple junction; however, an example of when this is not sufficient is for diffusivity along grain boundaries. As diffusivity is path dependant, a local connectivity descriptor such as TJFs may not capture the full information needed to accurately predict the macroscopic, or ensemble, material property [1].

We will use Fig. 1 as an example throughout this paper. Both microstructures in Fig. 1 have identical TJFs, calculated as the fraction of triple junctions with 0, 1, 2, or 3 special boundaries, but there is a non-negligible difference in D_{eff}, the effective,

---

[*] Corresponding author.

Email address: `cwa367@byu.edu` (C.W. Adair).

or ensemble, diffusivity, calculated using a previously derived, high-contrast model [1]. Therefore, there must be an underlying structural difference that causes the property difference.

While we give diffusivity as a specific example, there are varied applications where studies seek to understand long range effects of grain boundaries. Recent work in thermomechanical processing used coincident site lattice (CSL) labels and twin-related domains with maximum random boundary connectivity (MRBC) to characterize GBN effects on corrosion [5]. Another study on corrosion finds that conditions at boundaries affect corrosion severity through interrupting or allowing connected pathways [6].

The creep response of materials at high temperatures has also been shown to improve through addition of specific nanograin stable GBNs [4]. This method used TEM, CSL, and twin boundary characterization to visually identify specific GBN length structures that reduced high temperature creep, opposite to common grain boundary behavior at high temperatures.

Other mechanisms such as fracture and percolation can be modeled with higher fidelity by understanding the full connectivity of grain boundaries through materials [2, 5, 7–11]. Studies such as these rely on percolation theory and local measures such as TJFs to determine failure criteria, but the configuration spaces of these models are difficult to exhaustively search and test for failure conditions.

To overcome this limitation, recent studies seek to create automatable, quantitative analysis of highly connected components in materials. A field of math that has shown success in achieving this is Spectral Graph Theory (SGT), which allows for analysis of sets of vertices, edges, and properties on both [1, 12]. This has been applied in grain growth simulations to quantify anisotropy, and to identify and characterize abnormal grain growth [12].

The method used to calculate effective diffusivity in Fig. 1 uses SGT, with a high contrast diffusivity model, to encode network length grain boundary features and generate material property predictions, derived in previous work [1]. SGT in this implementation uses the Laplacian matrix representation of a meshed GBN, which encodes the full connectivity information of the individual boundaries [1]. The eigenvalues and eigenvectors of this matrix form the *spectrum* of the meshed microstructure.

In our prior work [1], a single eigenpair was selected from the spectrum of a GBN that represented the dominant microstructural feature contributing to the effective, or ensemble, diffusivity. This feature can be mapped back onto the mesh of the microstructure to visualize and qualitatively characterize the feature as either the dominant diffusive path or the barrier to diffusion, depending on the gradient of values [1]. However, this single eigenpair is, by nature, a truncation of the total information provided by the decomposition of the Laplacian matrix.

In this paper, we show that a variation of this harmonic Laplacian representation of GBN diffusion, which uses all eigenpairs, can enable deeper structural characterization for a broad range of GBN configurations. We do this by:

1. Deriving a PDE representation of diffusion on GBNs
2. Deriving a harmonic expansion representation of the diffusion PDE
3. Developing a difference measure between two microstructures based on this harmonic representation
4. Showing that the harmonic representation encodes long-range GBN structure

Using these methods, we show how a harmonic solution for GBNs can remove structure-property ambiguity by testing if microstructures that are well-separated in TJF space are also distinct in harmonic space (explaining the dramatic differences in properties for microstructures that are identical according to local structural descriptors, such as those shown in Fig. 1). Also, by studying spatial clustering in the harmonic representation space, we identify structural classes of GBNs, that were undetectable using previously available tools, and which explain differences in observed effective properties.

2. Methods

2.1. Derivation of the GBN Diffusion PDE

Consider the general form of the diffusion equation:

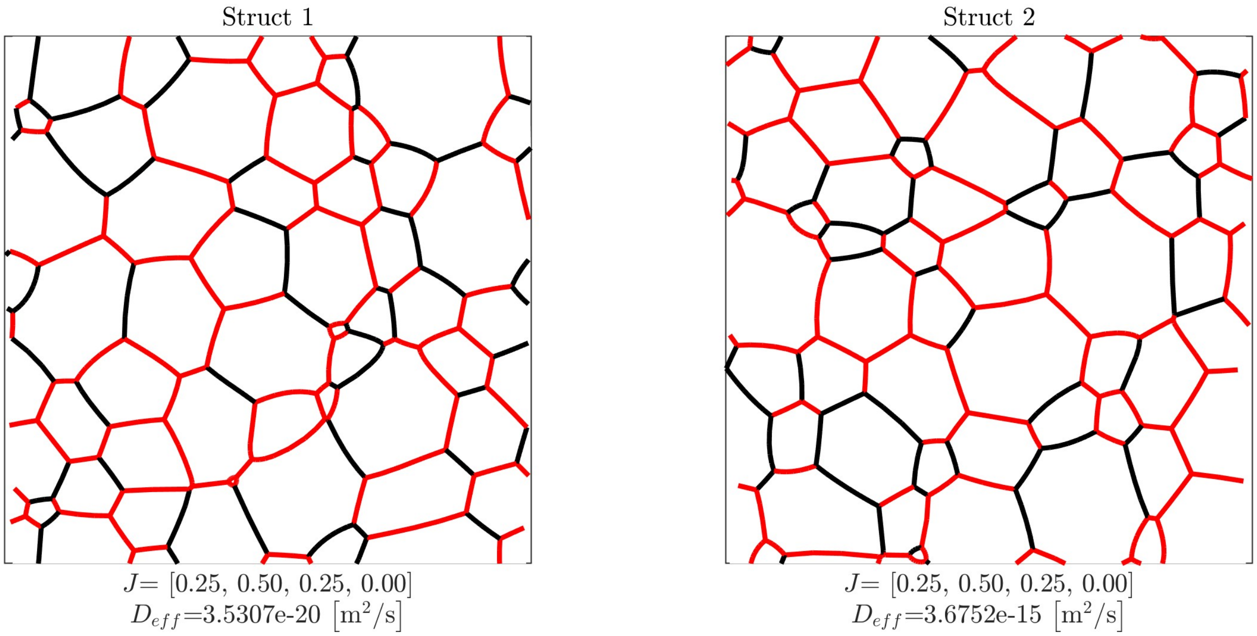

Struct 1

J= [0.25, 0.50, 0.25, 0.00]
D_{eff}=3.5307e-20 [m^2/s]

Struct 2

J= [0.25, 0.50, 0.25, 0.00]
D_{eff}=3.6752e-15 [m^2/s]

Figure 1: Example of two microstructures with identical TJFs, but very different effective diffusivities.

$$\frac{\partial C(r,t)}{\partial t} = \nabla \cdot [D(C,r)\nabla C(r,t)] \tag{1}$$

where C is the concentration of the diffusing species, r is the position vector, D is the diffusion coefficient, and t is time. Solving this equation yields an expression for the the concentration field $C(r,t)$. In the present case, we are interested in steady state diffusion, and we consider situations in which the diffusion coefficient is not concentration dependent. Under these conditions, Eq. 1 can be simplified to:

$$0 = \nabla \cdot [D(r)\nabla C(r)] \tag{2}$$

where $D(r)$ makes explicit the position dependence of the diffusion coefficient. Applying the product rule we obtain

$$0 = D(r)\nabla^2 C(r) + \nabla D(r) \cdot \nabla C(r) \tag{3}$$

where ∇^2 is the Laplacian operator.

We impose Dirichlet boundary conditions in the horizontal direction (X), and periodic boundary conditions in the vertical direction (Y), and we restrict our attention to the kinetic type-C regime, in which intergranular diffusion dominates (i.e. diffusion occurs only along the GBN) [1, 13, 14].

To numerically solve Eq. 3 in this context, we discretize the GBN into vertices and edges, thereby constructing a graph representation of the GBN, following the methods of Johnson et al. [1]. An example of this GBN discretization with the specified boundary conditions is shown in Fig. 2, where i and j are neighboring vertices connected by an edge.

The discrete representation of GBNs requires the assumption that between two vertices i and j the grain boundary length, area, and diffusivity remain constant. This means that that on e_{ij}, $\nabla D = 0$, which further simplifies Eq. 3 to:

$$0 = D\nabla^2 C \tag{4}$$

A weighted undirected graph, $G = (V, E, w)$, is defined by the set of vertices, V, the set of edges, E, and the corresponding set of edge weights, w [15]. Calculus operations exist in graph contexts, and allow for discrete analogs of continuous operators[16]. The weighted graph Laplacian is the discrete analog of the Laplacian operator, and is defined as

$$(\mathrm{div}_w(\nabla_w f))(x_i) = \sum_{x_j \sim x_i} w(x_i, x_j)(f(x_j) - f(x_i)) \tag{5}$$

where x_i is a vertex of G, and the sum is over all vertices, x_j, that share an edge with x_i (denoted

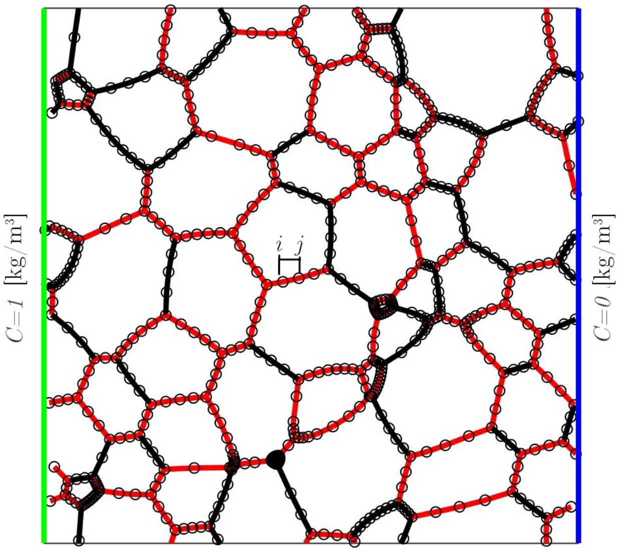

Figure 2: Example of a GBN discretization and the boundary values. The color of the interior edges represent D_{ij}, red for 10^{-8} m^2/s, and black for 10^{-15} m^2/s. The green edge represents the diffusion source, and the blue edge the diffusion sink. The upper and lower edges are periodic.

$x_j \sim x_i$), and f is the function of interest on the vertices, which, for our purposes, corresponds to C, the nodal concentrations.

Assuming constant properties on edges results in a weighting function of the form $w_{ij} = D_{ij}L_{ij}/A_{ij}$, following a finite volume representation, where D is the diffusivity assigned by the constitutive model to that edge, L is the length of the edge, and A is the cross-sectional area of the grain boundary, which we set to be constant [1]. The diffusivity of a grain boundary will be modeled with a simple bimodal high-contrast constitutive model for special and general grain boundaries [1, 7, 17, 18]. The constitutive model we use will assign to special boundaries (<15° disorientation angle) a low diffusivity ($10^{-15}\,\mathrm{m^2/s}$), and to general boundaries (≥15° disorientation angle) a high diffusivity ($10^{-8}\,\mathrm{m^2/s}$). The ratio between low- and high- diffusivity was chosen to be consistent with reported differences in kinetic type-C diffusion and boundary diffusion differences in experiments [14, 18, 19].

In matrix form the Laplacian can be constructed as

$$\mathcal{L}_{ij} = \begin{cases} \displaystyle\sum_{i\sim m} \frac{D_{im}A_{im}}{L_{im}} & \text{if } i = j \\ -\dfrac{D_{ij}A_{ij}}{L_{ij}} & \text{if } i \sim j \\ 0 & \text{otherwise} \end{cases} \tag{6}$$

Note that the diffusivity is now included directly in the weighted graph Laplacian.

Eq. 4 can now be written in the discrete form:

$$\mathcal{L}C_n = 0 \tag{7}$$

where C_n is now a vector of length n, where n is the number of vertices in G, and is the vector containing the concentrations at the graph vertices, and $\mathcal{L}$ is the weighted graph Laplacian defined in Eq. 6.

Adding the Dirichlet boundary conditions requires new definitions: The subset of vertices $\delta F \subset V$, called the exterior set, and $F \subset V$, which is the interior set. Note that $F \cup \delta F = V$. For simplicity in calculations, vertex indices on the left surface of each microstructure are reassigned a single vertex index, called the source vertex, set at an arbitrary concentration of $1\,\mathrm{kg/m^3}$, and vertex indices on the right surface are combined into a single sink vertex set at $0\,\mathrm{kg/m^3}$.

Visualization of these conditions can be seen in Fig. 2. The edge weight information and results remain unchanged by this index reassignment, it merely simplifies the math required for calculations. The source and sink vertices are part of the exterior set, while all others are part of the interior set. The vertices can be ordered in such a way as to partition the vector C_n into the concentrations on the exterior vertices—which are set by the boundary conditions—and the concentrations on the interior vertices—which are unknown. This also results in a corresponding partition of the weighted Laplacian. The Dirichlet boundary conditions can now be included explicitly by augmenting the system of equations in Eq. 7, creating the following boundary

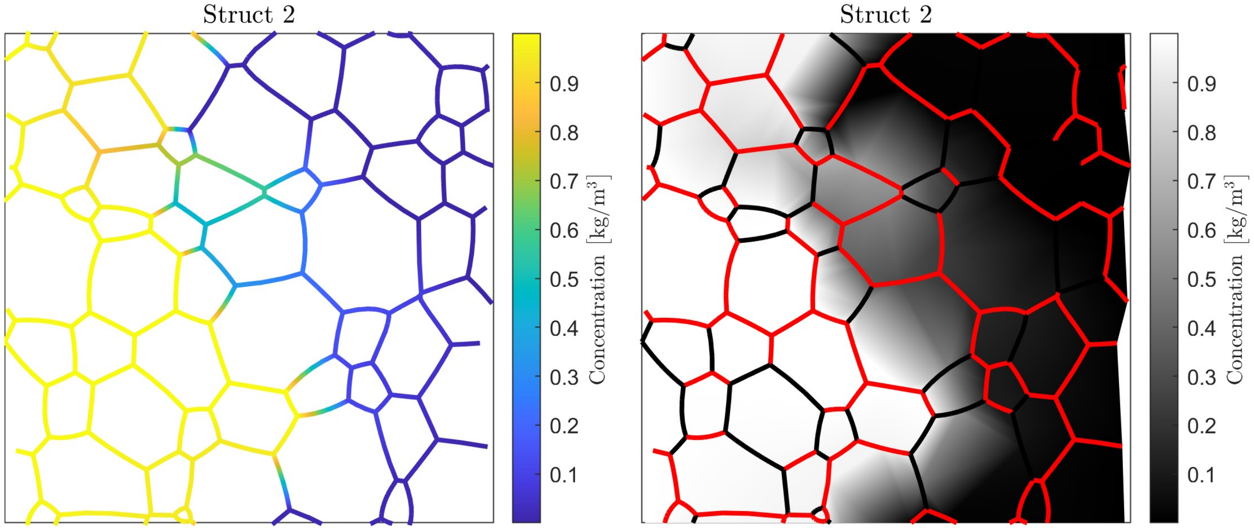

Figure 3: The concentration solution, C_n, for structure 2 shown in Fig. 1. The left figure shows the concentrations on the mesh as modeled, while the right shows the interpolation of C_n so boundary properties can be seen alongside concentration. A reminder that there is no diffusion through the bulk in this model.

value problem:

$$\left[\begin{array}{cc|c} 1 & 0 & 0 \\ 0 & 1 & \\ \hline L_{n\times\delta F} & & L_{n\times n}\end{array}\right] \begin{bmatrix} c_{source}\\ c_{sink}\\ c_1\\ c_2\\ \vdots\\ c_n\end{bmatrix} = \begin{bmatrix} c_{source}\\ c_{sink}\\ 0\\ 0\\ \vdots\\ 0\end{bmatrix} \tag{8}$$

where $L_{n\times\delta F}$ is the sub-matrix of $\mathcal{L}$ corresponding to the edges between the interior (F) and exterior (δF) vertices $(e_{ij} : i \in \delta F \text{ and } j \in F)$, $L_{n\times n}$ is the sub-matrix corresponding to the edges between interior vertices, and c_i are the vertex concentrations. Eq. 8 can be recast into a convenient form by first carrying out the blockwise matrix multiplication

$$L_{n\times n}C_n + L_{n\times\delta F}\begin{bmatrix} c_{source}\\ c_{sink}\end{bmatrix} = \begin{bmatrix} 0\\ \vdots\\ 0\end{bmatrix} \tag{9}$$

and then solving for $L_{n\times n}C_n$ to obtain

$$L_{n\times n}C_n = B \tag{10}$$

with

$$B = -L_{n\times\delta F}\begin{bmatrix} c_{source}\\ c_{sink}\end{bmatrix} \tag{11}$$

As B is constant for a given microstructure and set of boundary conditions, Eq. 10 can be recognized as a Poisson equation, the more general inhomogeneous version of the Laplace equation [16]. Eq. 10 can now be solved using standard matrix methods to obtain the values of the concentration field evaluated at each interior vertex (i.e., $C_n : V \to \mathbb{R}_{\geq 0}$ is a function over the vertex set) [16].

The concentration vector can be visualized using the GBN mesh as shown in Fig. 3. To enable simultaneous visualization of the spatial distribution of GB properties and C_n, we interpolate the values of C_n across the grains (right panel of Fig. 3). This is only for visualization, however, as *there is no diffusion through the crystal bulk in this model.*

This visualization allows us to see *qualitative* correlations between GBN structure and long-range diffusion. However, $L_{n\times n}$, C, and B are not directly usable for *quantitative* comparisons between microstructures in their current form. For that we turn to Spectral Graph Theory, and the ideas of harmonic functions and domains.

2.2. Harmonic Representation of the PDE Solution

Spectral Graph Theory is the study of eigenvectors of the matrix representations of graphs (such

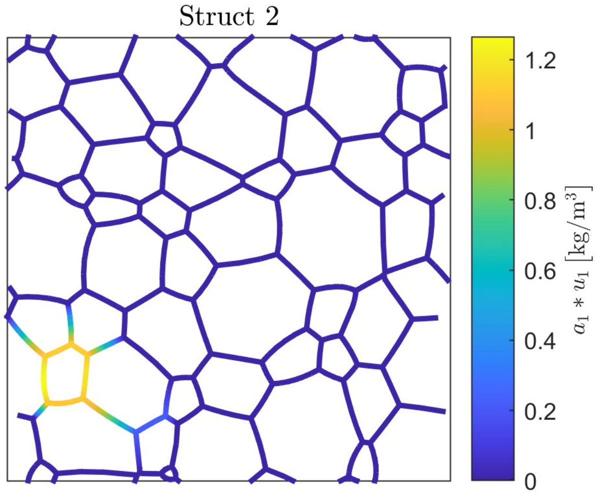

Figure 4: Example of an eigenvector term from Eq. 14 projected onto the GBN.

as the graph Laplacian, $\mathcal{L}$), and has recently been applied to the problem of intergranular diffusion [1]. In contrast to the previous study, the derivation of Eq. 10 formulates the diffusion problem as an inhomogeneous partial differential equation, where the relevant matrix representation is $L_{n\times n}$, in contrast to $\mathcal{L}$ [1].

While $\mathcal{L}$ is singular, $L_{n\times n}$ is non-singular. We can therefore obtain the interior vertex concentrations from Eq. 10 by inversion:

$$C_n = L_{n\times n}^{-1} B \tag{12}$$

The matrix $L_{n\times n}$ admits the spectral decomposition $L_{n\times n} = U\Lambda U^{-1}$, where Λ is the diagonal matrix containing the eigenvalues of $L_{n\times n}$, $\lambda_1 \leq \lambda_2 \leq \cdots \leq \lambda_n$, sorted in ascending order, and U is the matrix whose columns comprise the corresponding eigenvectors. Substituting this expression into Eq. 12 we obtain

$$\begin{aligned} C_n &= \left(U\Lambda U^{-1}\right)^{-1} B \\ C_n &= U\Lambda^{-1}U^{-1} B \end{aligned} \tag{13}$$

and letting $A = \Lambda^{-1}U^{-1}B$ we obtain

$$\begin{aligned} C_n &= UA \\ &= \sum_k a_k u_k \end{aligned} \tag{14}$$

where a_k is the k-th element of the vector A defined above, and u_k is the k-th eigenvector of $L_{n\times n}$ (i.e., the k-th column of U). Eq. 14 represents a harmonic series expansion of C_n, where the u_k are the basis "functions" and the a_k are the corresponding coefficients. As the u_k are defined uniquely only up to a sign, we choose, as a convention, the sign that ensures $a_k \geq 0 \ \forall \ k$.

The eigenfunctions, $u_k : V \to [-1, 1]$, represent the eigenmodes of the microstructure for the diffusion problem, and these can be visualized most clearly in the same way that we first visualized C_n, as a color gradient on the vertices and edges of the GBN, as shown in Fig. 4.

2.3. Quantifying GBN Diffusion Response

While the spectral decomposition in Eq. 14 gives quantitative parameters (the a_k) that relate GBN structure to macroscopic performance, they still cannot be directly used for similarity or difference comparisons.

If two microstructures had exactly the same sets of eigenfunctions (u_k), then comparisons could be made simply using the L^2-norm of the difference between their A vectors. However, since the domain of the eigenfunctions (u_k) is explicitly tied to a specific GBN discretization (V), different GBNs may exhibit different harmonics (u_k). This is similar, in part, to Fourier transforms applied over different spatial domains, where the specific basis functions for a plane and a disk are different [20]. Therefore, direct comparisons of A are not guaranteed to be comparisons of equivalent eigenmodes.

However, a similar problem exists in signal analysis of musical instruments [21, 22]. While the geometry of different musical instruments vary widely, meaningful comparisons can still be made on the basis of their frequency response (i.e., the way they sound) [22].

The spectral formulation employed to obtain Eq. 14 enables the definition of the power spectrum of C_n for each microstructure, which is simply

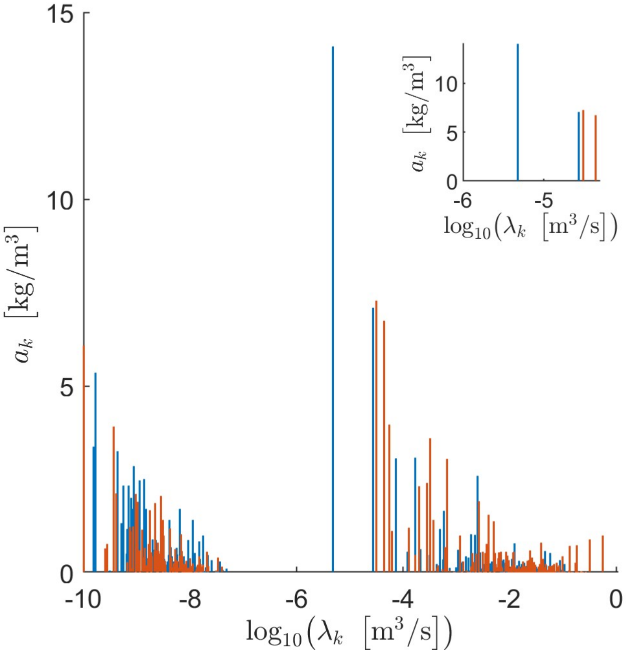

Figure 5: Discrete power spectra of the GBNs shown in Fig. 1. Note the differences and similarities in peak heights and locations.

a plot of a_k vs. λ_k, where the eigenvalues indicate the spatial frequency of the corresponding eigenmode[1,2]. As an example, Fig. 5 shows the power spectrum of the microstructures from Fig. 1.

From Fig. 5 we can already begin to see the usefulness of this representation. Although the two microstructures in Fig. 1 are indistinguishable using traditional structure metrics (the TJFs), the power spectrum reveals that the dominant eigenmodes of the two microstructures correspond to different spatial frequncies.

2.4. Quantifying GBN Difference

To compare microstructures quantitatively using their power spectra requires the definition of a distance or difference measure. Such a difference measure should have a small value for two microstructures with similar power spectra, and a large value for two microstructures with very different power spectra.

The power spectrum can be seen as a set of Dirac delta functions of amplitude a_k located at λ_k. The discrete nature of these power spectra makes direct comparisons overly strict. For example, in the inset of Fig. 5, there are two peaks with similar frequencies ($\log_{10}(\lambda) \approx -4.6$) and amplitudes, but since they are not exactly equal a Euclidean distance will not result in a small contribution to the total distance as expected. We would expect that the well separated peak from Structure 1 in the inset denotes a distinct feature and should contribute to a large difference, but we would expect that features close together, like the almost matching peaks, would contribute a difference close to zero. Moreover, direct comparison of two discrete power spectra that are identical at all points but shifted horizontally by an infinitesimal amount relative to one another would yield as large a distance as two power spectra that are completely unalike.

A solution that corrects for this discretization effect is to replace the discrete power spectra with continuous ones by spreading out each peak. We do this by replacing each peak in the discrete power spectrum with a Gaussian of amplitude a_k, centered at the corresponding λ_k, and having a standard deviation of σ (see Fig. 8).

The value of σ is chosen to be a single universal value of $\sigma = 0.05$ for all microstructures, determined by a sensitivity analysis of σ vs. continuous power spectrum distance, with the distance defined by

$$d(A_1, A_2) = \sqrt{\sum_i \left[A_1(\lambda_i) - A_2(\lambda_i)\right]^2} \qquad (15)$$

where the λ_i are a universal set of quadrature points. The optimal value of σ was selected to be as small as possible while ensuring that the inter-spectrum distances are stable against small perturbations of σ (see Appendix A).

3. Results

Using an existing library of 1771 2D microstructures [2] having TJFs that spanned the TJ config-

---

[1] The usual definition of a power spectrum would employ $|a_k|^2$; however, since $a_k \geq 0 \;\forall\; k$ there is no practical difference and we refer to a_k vs. λ_k as the power spectrum.

[2] Because the values of D_{ij} are small, for numerical stability we scale the edge weights in $L_{n\times n}$ by a factor of 10^{15}. Consequently the values of the λ_k are scaled by the same factor.

uration space, we calculated the $A(\lambda)$ (i.e., the C_n power spectra) for each as described in Sections 2.3 and 2.4.

3.1. The Eigenvalue Spectrum Encodes GBN Structure

In Fig. 6, we present the eigenvalue spectra for a diverse set of microstructures. This set includes the bounds of all eigenvalue spectra, so all microstructures fall between these values. A notable feature common to all of the spectra is a spectral gap or jump, where the eigenvalues of a single microstructure have a large discontinuity.

At first glance, the index of the eigenvalue jump appears to correlate with the fraction of low-angle grain boundaries (LAGBs). This correlation holds for all of the microstructures considered here, as shown explicitly in Fig. 7. Therefore, the eigenvalue spectrum encodes the boundary composition of a microstructure.

However, even for two microstructures with nearly identical eigenvalue spectra there are distinct differences between the boundary configurations, concentration gradients, and even D_{eff} (compare the pairs of microstructures in the top-left and top-right of Fig. 7).

The configurational differences are encoded in U, the eigenvectors of each microstructure. Fig. 9 illustrates this. For a given eigenpair, if λ_k is lower than the spectral gap then u_k has gradients along connected sections of LAGBs, and if λ_k is above the spectral gap then u_k has gradients along connected section of HAGBs. U, the full set of eigenvectors, describes the set of all connected (or isolated in the case of the third eigenpair of Struct 1) sections of grain boundary types that exist in a given microstructure. However, we do not know from U alone which configurational attributes/features contribute the most to performance.

3.2. The Power Spectrum Encodes the Structure-Property Relationship

In Eq. 14 we defined the performance (C_n), the structure (U), and the link between the two (A). Using our original example from Fig. 1, we can show how the power spectrum can be used to distinguish different GBNs, and identify the underlying configurational causes of those differences, as illustrated in Fig. 8.

First, both microstructures in Fig. 8 have identical TJFs, but very different D_{eff}, which shows the presence of a long range effect. Second, both have very similar eigenvalue spectra, which from Section 3.1 means that the large property difference is not caused by differences in LAGB length fractions, but by a configurational difference (i.e. specific eigenvectors in U).

By using the power spectra formulation of Eq. 14, we can now identify eigenmodes that dominate the performance of the respective GBNs and explain their difference. Both power spectra exhibit the spectral gap between low and high eigenvalues from the eigenvalue spectra, but the peak heights (a_k) show that structure 2, the high D_{eff} example, exhibits stronger high λ_k eigenmodes than structure 1.

By selecting the 3 most dominant eigenvectors of each microstructure, we can visualize the eigenvectors on the GBN mesh, as shown in Fig. 9. Of immediate note, the eigenvectors with frequencies above the spectral gap show gradients along the high-angle grain boundaries (HAGBs), while subgap eigenvectors show gradients along the LAGBs. This follows the behavior expected of a spectral embedding, where spectral distance between two vertices is inversely related to the weight of the edge connecting them [23]. Thus, high frequency eigenmodes exhibit gradients along the high-weight edges (in this case the HAGBs), and vice-versa.

The eigenvectors also highlight distinct features of the respective GBNs (see Fig. 9). For structure 1 the three most dominant eigenmodes highlight, respectively, (i) the primary barrier to percolation at the perimeter of a HAGB cluster, (ii) the most connected section of HABGs, and (iii) a local grouping of LAGBs. The dominant eigenmodes of structure 2 highlight, respectively, (i) a cluster of HAGBs leading to the deepest high-concentration diffusion front, (ii) the percolating set of HAGBs, and (iii) a local set of LAGBs.

In both cases, the two highest peaks in the respective power spectra occur above the spectral

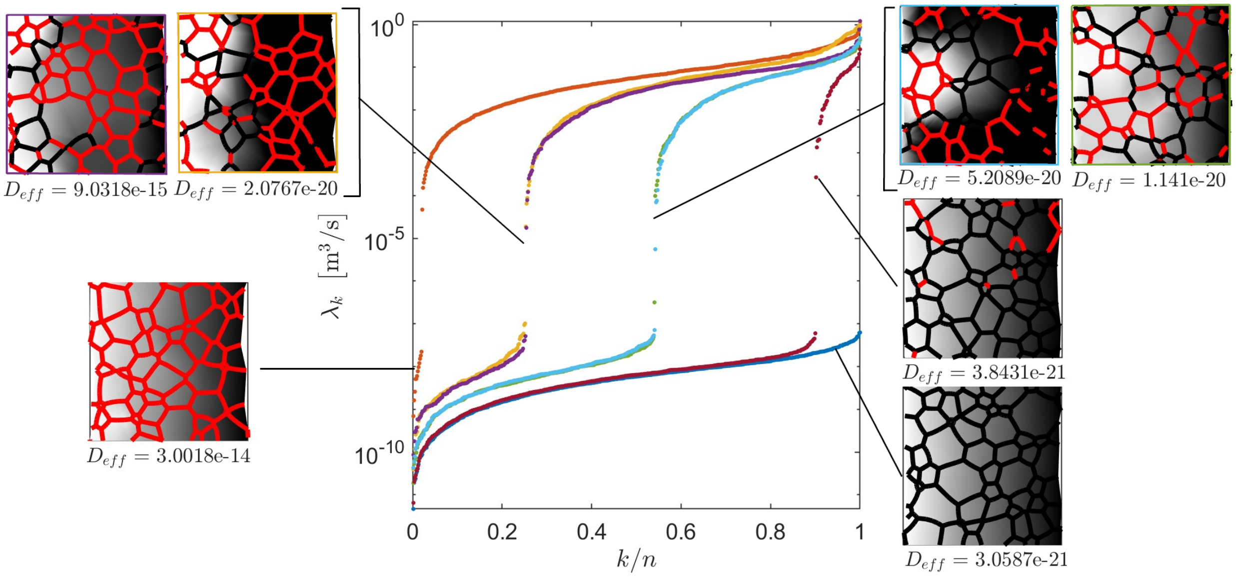

Figure 6: Example microstructures and their corresponding eigenvalue spectra. D_{eff} units are in m^2/s

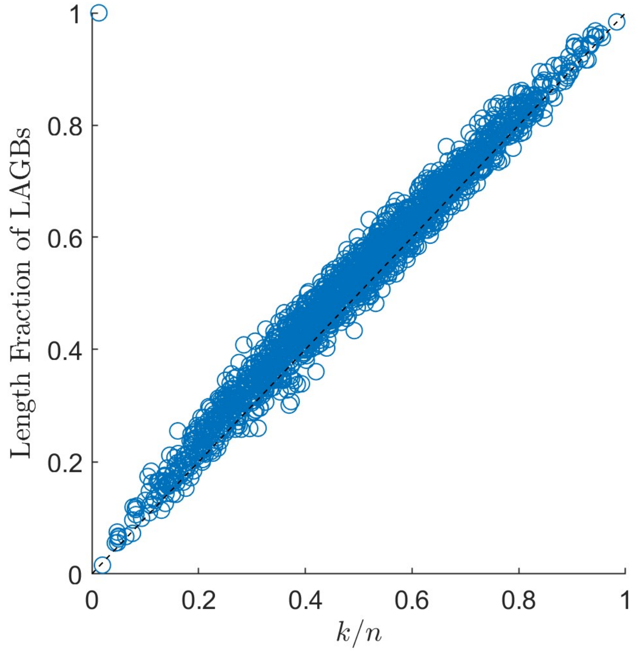

Figure 7: Correlation of the length fraction of low angle grain boundaries against the normalized eigenvalue jump index. Dashed line given for 1 to 1 reference.

gap, and therefore highlight configurational differences related to HAGB clusters, whereas the third highest peak occurs below the spectral gap and therefore highlights an important configuration of LAGBs.

Although insightful, a visual comparison of eigenmodes across all 1771 microstructures would be infeasible. To identify overarching trends across the large library of microstructures, we require a numerical difference or distance measure between GBNs, which the power spectrum also furnishes.

3.3. Power Spectrum Classification of GBNs

As there are a large number of pairwise comparisons in our dataset we turn to clustering to help classify and understand the trends and features of our microstructures. Since we do not know the number of clusters a priori, we turn to unsupervised clustering to identify broad similarities and differences.

We use affinity propogation (AP) clustering with the elements of the similarity matrix defined by

$$s_{ij} = -d(A_i, A_j) \tag{16}$$

and the exemplar preference defined by the median similarity of each spectrum to all others (i.e., the exemplar preference of the i-th spectrum is given by the median of the i-th row of s) [24]. An exemplar

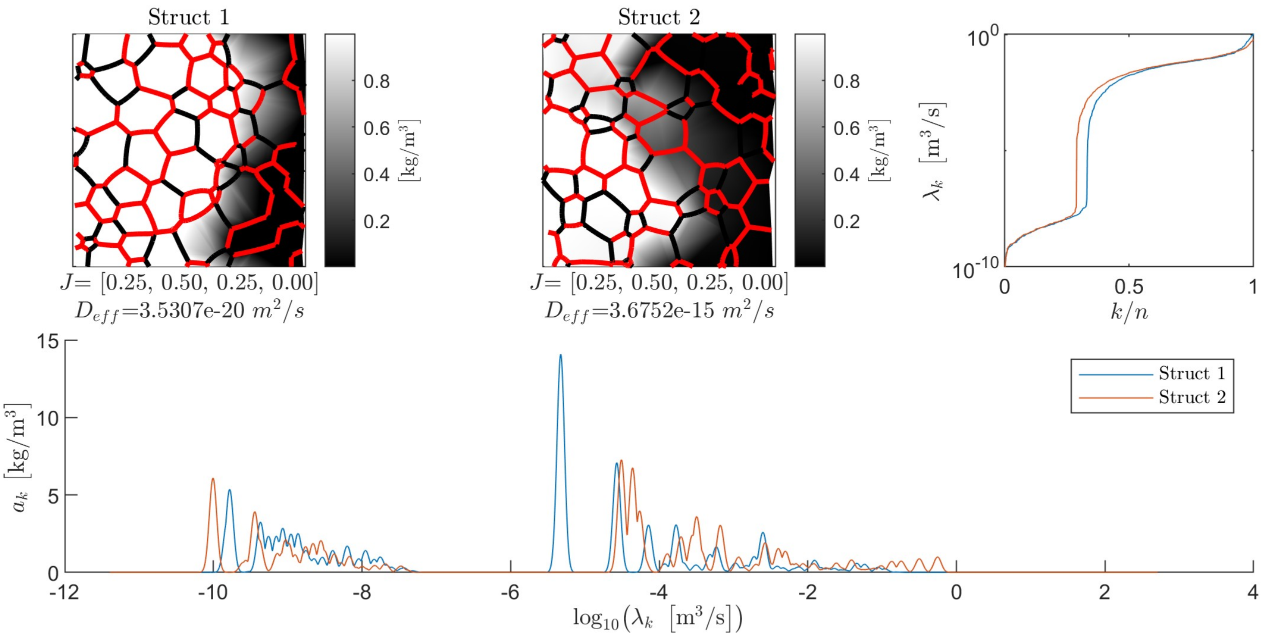

Figure 8: Structures 1 and 2 from Fig. 1 (top left), together with their respective eigenvalue spectra (top right) and power spectra (bottom). Though both structures have identical TJFs and nearly identical eigenvalue spectra, the power spectrum shows that there are differences in the dominant eigenmodes, which explain the differences in concentration profiles and effective properties.

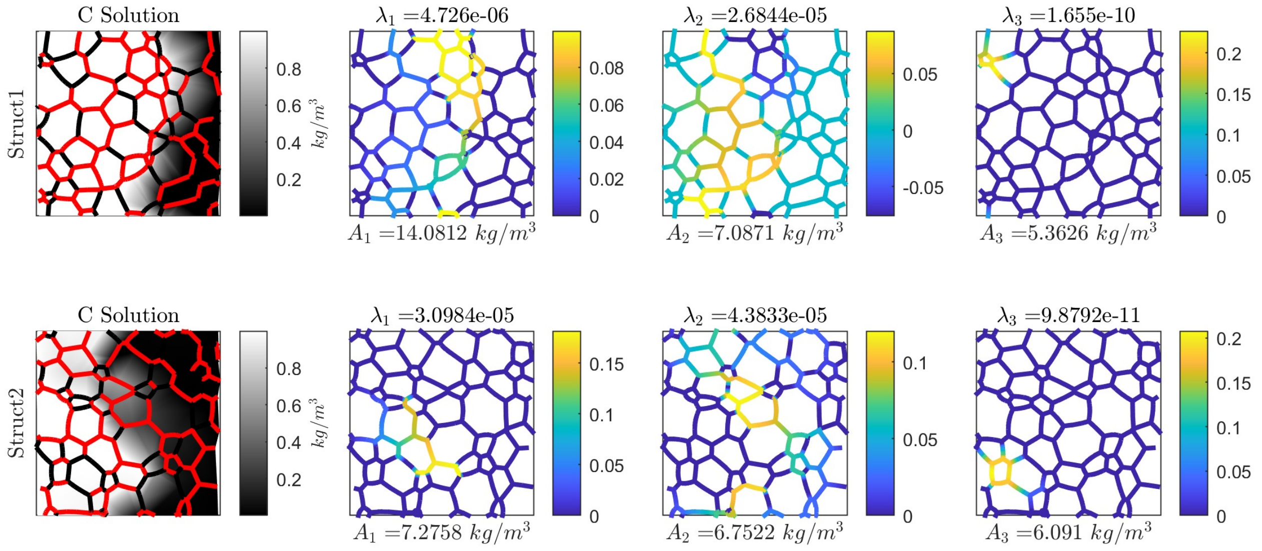

Figure 9: Visualization of the 3 most dominant eigenmodes for the two structures from Fig. 1. Note the locations of the gradients in the eigenvectors.

is a member of the cluster that falls near the center of the cluster, and will be used as a reference point representing that cluster.

AP clustering found 117 clusters from the 1771 microstructures. These can be visualized by sorting the pairwise distance matrix by cluster, colored by $d(A_i, A_j)$, as shown in Fig. 10. Each black square shows the bounds of the clusters found.

Since most clusters have values close to 0 within the squares, and values much higher than 0 outside the square but in the same row/column, the clusters are generally well-formed, or well separated from each other. However, certain clusters in Fig. 10, such as those in the bottom right, are very similar in value to surrounding clusters as evidenced by low $d(A_i, A_j)$ values in the same rows. This can happen due to misclassification error from AP as a result of the unsupervised nature of this clustering algorithm.

To validate the separation of clusters, we can use the exemplar of each cluster as reference points for mean comparisons. For example, given a single cluster exemplar, we expect that microstructures in the exemplar's cluster would have $d(A_{exemplar}, A_j)$ near 0, while the distance from the exemplar to all other microstructures would be far from 0. Therefore, we would also expect that the mean $d(A_{exemplar}, A_j)$ for all microstructures in the exemplar's cluster to be close to 0, while the mean $d(A_{exemplar}, A_j)$ for all other microstructures be significantly larger.

If we use the cluster ID assigned by AP as a grouping variable, we can use ANOVA and Tukey-Kramer (HSD) post-processing to identify if, *for a given exemplar*, there are specific overlapping clusters. We can repeat this process for all 117 cluster exemplars to find if this significant mean separation holds true for each cluster.

ANOVA reveals that most clusters are well formed at the 0.01 significance level, with all exemplars having at least one significantly different cluster mean. Using Tukey-Kramer (HSD) post-processing, out of the 13,689 mean comparisons to exemplars grouped by cluster label, 13,488 were found to be significantly different at the 0.01 level as illustrated in Fig. 11. Therefore, 98.53 % of cluster pairs were found to be well separated, with 98.01 % found significant at 0.001 level.

To spatially visualize the quality of the clustering, we used t-Distributed Stochastic Neighbor Embedding (t-SNE) on the continuous power spectra for dimensionality reduction. Fig. 12 shows the resulting 2D embedding with each point representing one of the 1771 microstructures, colored by cluster ID. The distance between any two points in Fig. 12 approximates the high-dimensional pairwise distance between the power spectra of the corresponding microstructures.

For clarity when discussing the clusters, we will focus on a subset of 55 clusters that represents the largest subset whose separations are jointly pairwise significant at the 0.01 significance level. Fig. 12 shows how this maximal subset removes much of the overlap between neighboring clusters.

4. Discussion

We found that spectral information of GBNs encodes structural and performance information that classical GBN descriptors could not, and that this new information could be used to identify distinct clusters in the harmonic space. Out of 117 clusters, a subset of 55 clusters formed a jointly pairwise significant subset. From this subset of clusters, we will show how this spectral information enhances our understanding of current GBN descriptors, and how the spectral structure informs the properties of microstructures.

4.1. Correspondence between Power Spectrum Clusters and Existing Structural Descriptors

From Fig. 8 we showed how two classical GBN descriptors, TJF and special boundary fraction, were insufficient to explain a structure-performance difference. We can use the t-SNE representation of the spectral clusters, first shown in Fig. 12, to visualize the general trends of both TJF and LAGB length fraction on the spectral clusters, as shown in Fig. 13. In the top panel of Fig. 13, the t-SNE points are colored according to the TJF color mapping shown in the tetrahedron, the middle panel is colored according to cluster, and the bottom panel is colored according to LAGB length fraction.

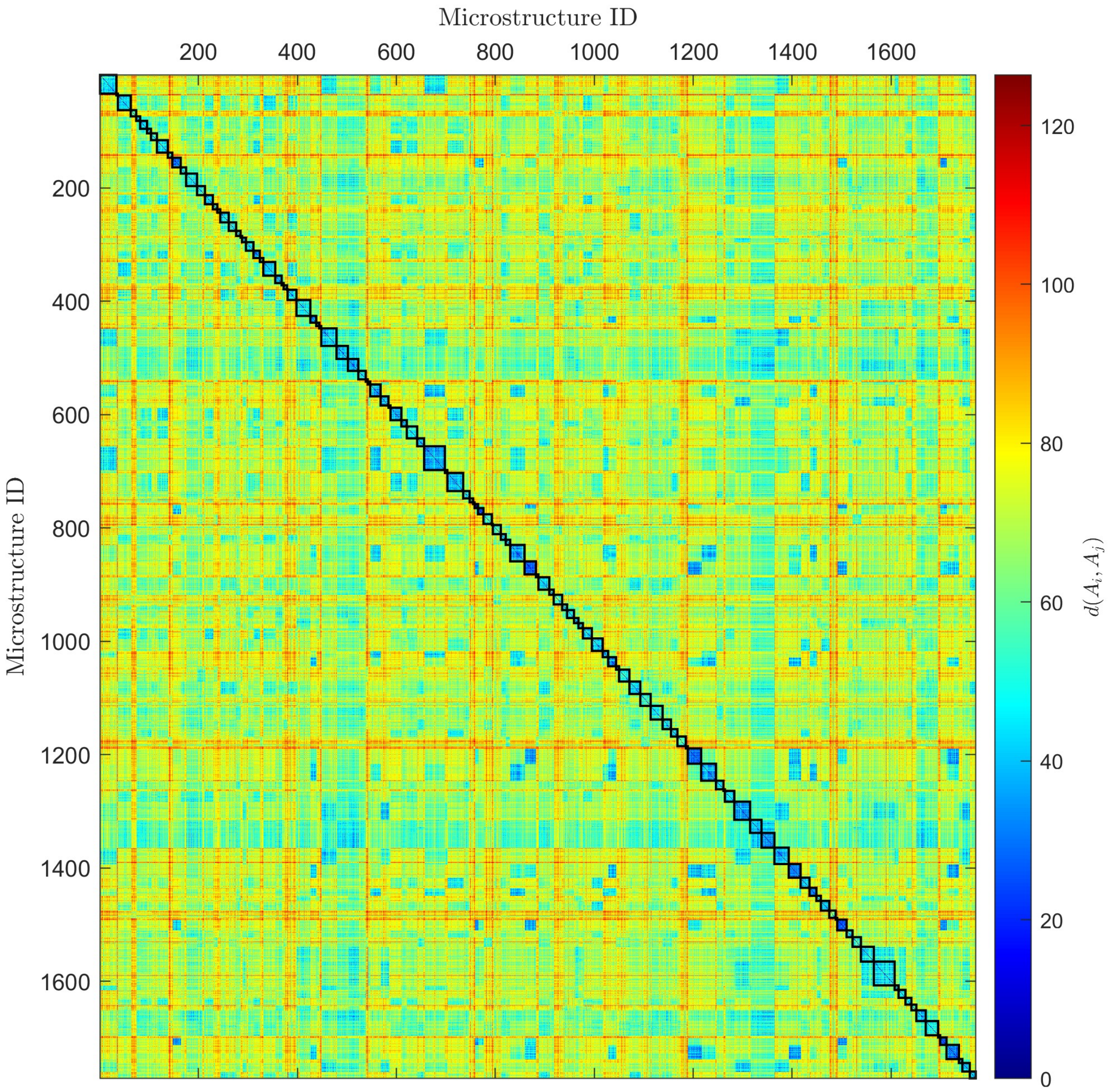

Figure 10: Distance matrix sorted by clusters found by AP. Each pixel corresponds to a single pairwise comparison.

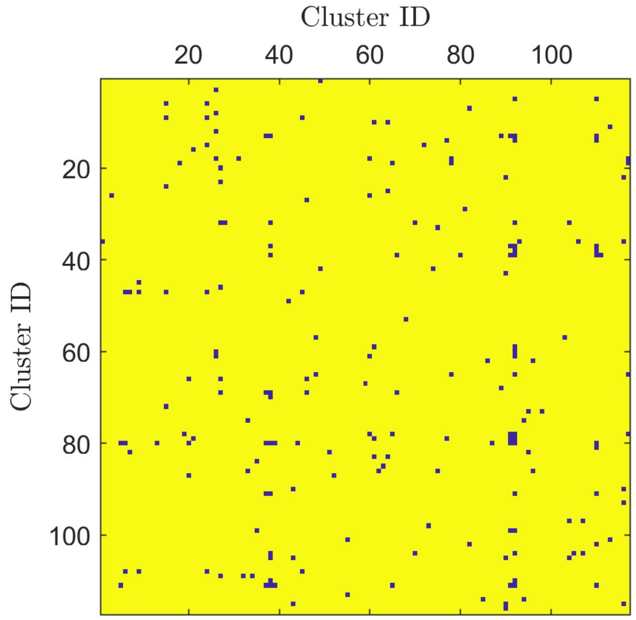

Figure 11: Significance at the 0.01 level found by HSD on the Cluster Means. Yellow indicates statistical significance at the 0.01 level, while blue indicates that the difference between clusters is not significant at this level.

Overall, the t-SNE embedding of the spectral information separates the J_3-J_2 corners (black-yellow) from the J_1-J_0 corners (pink-blue). The clusters themselves follow this trend, where clusters consist of a mixture of J_3-J_2 or J_1-J_0 TJ types. The J_1 corner (pink) and the center of the TJF tetrahedron (light gray), however, are spread out in the t-SNE embedding, with few concentrated sections of J_1 dominant microstructures. This is a clear example of when there are distinct clusters in harmonic space, but overlap in TJF space.

We show examples of this overlap in Fig. 14. The t-SNE embedding shows how some of these overlapping TJF clusters are also close in the embedding, but there are some clusters that are also distinctly separate. The power spectra of each cluster help show the reasons for the varying distances in the embedding space, where Clust 3 has a distinct high λ_k peak in a different location than Clust 2 and 4, but also has a distinct low λ_k peak that does not exist in Clust 1.

By analyzing the overlap of clusters in the TJF space in this way, we find that the J_1 corner and

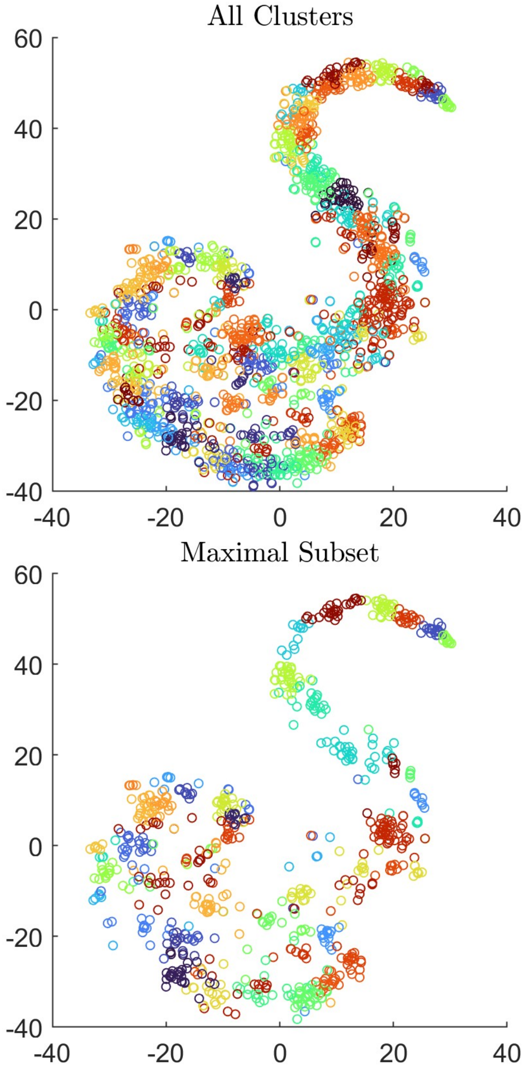

Figure 12: t-SNE using $d(A_i, A_j)$. All points are colored by cluster ID. The maximal subset represents the largest subset of clusters whose separations are jointly pairwise significant. Since the clusters are tightly grouped and there is limited color space, clusters that have similar colors, but are separated by distance, are distinct clusters.

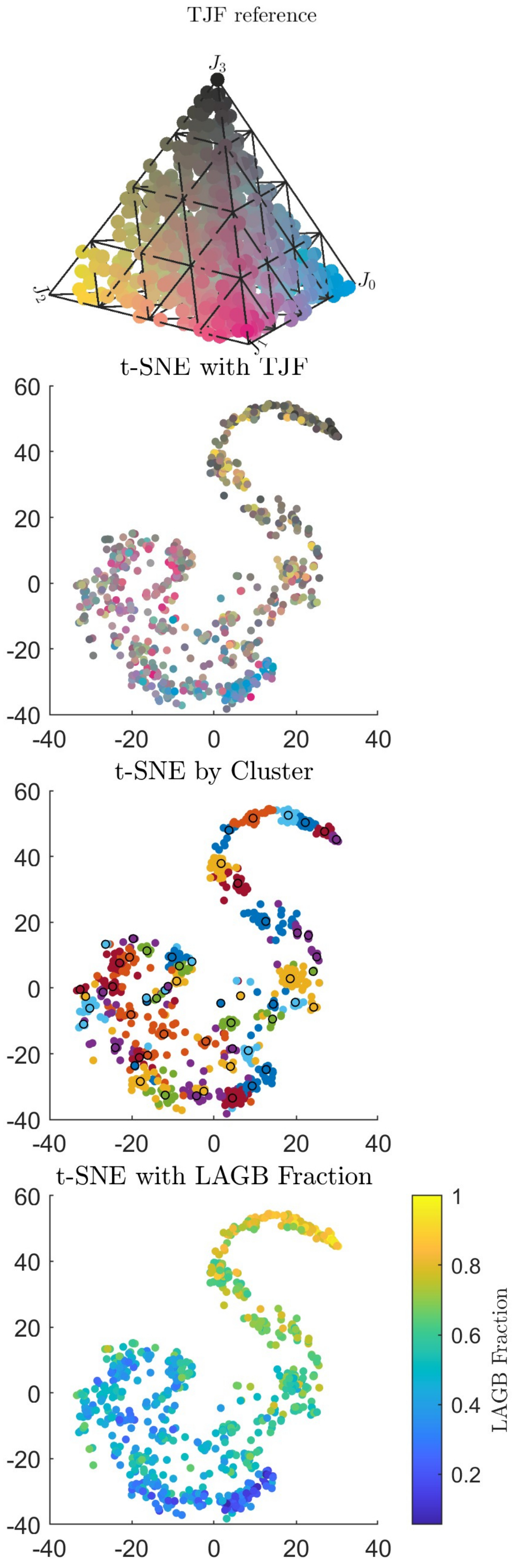

Figure 13: t-SNE embeddings for clusters, TJF, and special boundary fraction. Outlined markers in the cluster represent the exemplar of the cluster.

the center of the TJ tetrahedron are the most sensitive to configurational changes, while the J_2-J_3 edge is the least sensitive to configurational variations. That is, GBNs with equal numbers of all TJ types or a high population of J_1-type TJs might change cluster affiliation or have large changes in performance with the application of a small perturbation to their structure, whereas GBNs with a high population of J_2 and/or J_3-type TJs are stable against such perturbations (compare Figs. 13 and 15).

The correlations between t-SNE and the length fraction of LAGBs are similarly distinct in the embedding space. It is interesting to note that the spreading seen from the J_1 dominated structures correlate well with length fractions close to 0.5, while the extreme length fractions are more localized to the J_3 and J_0 dominated structures. Microstructures with near parity between LAGB length fraction and HAGB length fraction have more possible configurations than microstructures dominated by a single boundary type. Therefore, the presence of many distinct clusters with a LAGB length fraction of about 0.5 supports our observation that power spectra can differentiate boundary configurations, and that distinguishing GBNs near this LAGB length fraction requires more information than the two classical descriptors (p and J_i) provide.

4.2. Correlation between Power Spectrum and Performance

The two performance measures we consider as properties are D_{eff}, the effective diffusivity, and C_n, the concentrations at the vertices. With the new understanding of configurations from the spectral clustering method, we can better describe the underlying microstructural causes of differences in performance.

Using the same t-SNE embedding as previously discussed, we show how D_{eff} is distributed through the embedded harmonic space, shown in Fig. 15. The top tile shows the same cluster colorings as Fig. 13, the middle tile shows D_{eff} plotted on a logarithmic scale to show clearly when a HAGB percolating path exists, with yellow representing percolating microstructures and blue non-percolating,

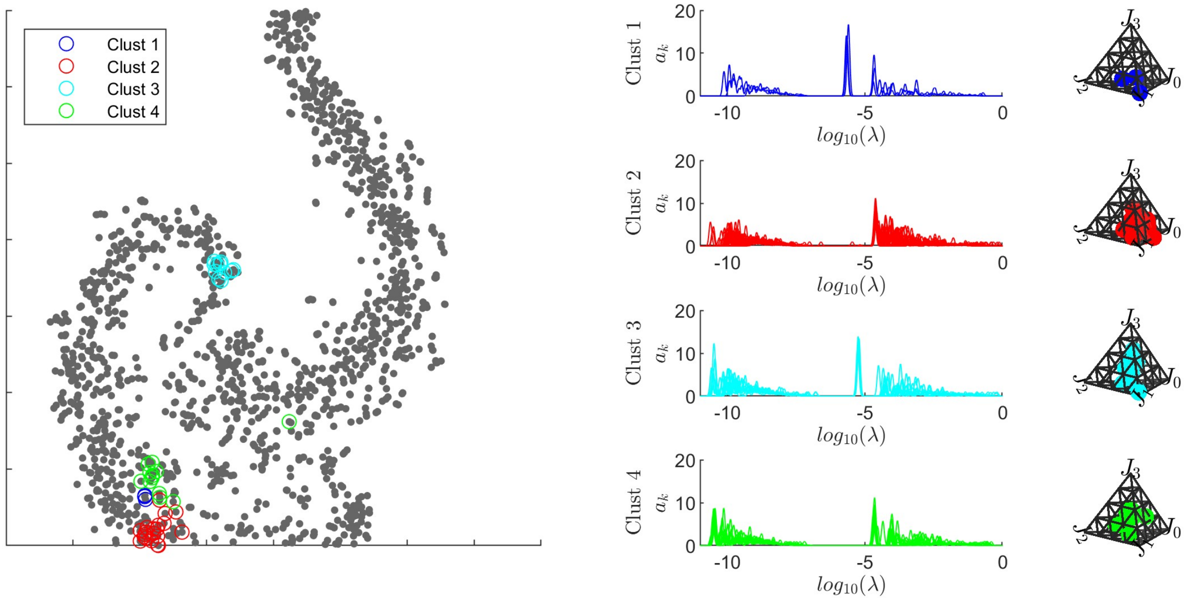

Figure 14: Examples of clusters that overlap in TJ space (near the J_1 corner), but have clear visual differences in power spectra, as well as similarities and differences in the t-SNE embedding. Note the similar locations and peak heights in the respective power spectra *within* clusters and the different locations and peak heights *between* clusters.

and the bottom tile showing the average of all vertex concentrations for each microstructure.

A previous study used three-body nearest-neighbor correlations to predict the percolating condition of microstructures, where the percolation threshold, p_c, of LAGBs was calculated from the TJFs [11]. The value of p_c for HAGBs can be calculated in the same way, and, since D_{eff} is dependent on the percolation of HAGBs rather than LAGBs, we use this HAGB version of p_c here. We can compare the actual HAGB percolation state of each microstructure (percolating or non-percolating HAGBs) to the state predicted from the J_i in this way (which encode only short-range correlations). When using the HAGB p_c predicted from the TJFs to predict percolation, we find 61 type 1 (false-positive) and 189 type 2 (false-negative) errors in this data set, as shown in Fig. 16. These are cases where long-range structure (beyond emergent structure based solely on local correlations) plays a definitive role in the effective properties of the GBN.

Since the p_c predicted in this way is informed only by local correlations, these errors may be caused by network level effects, which we can analyze using the power spectra. For a homogeneous

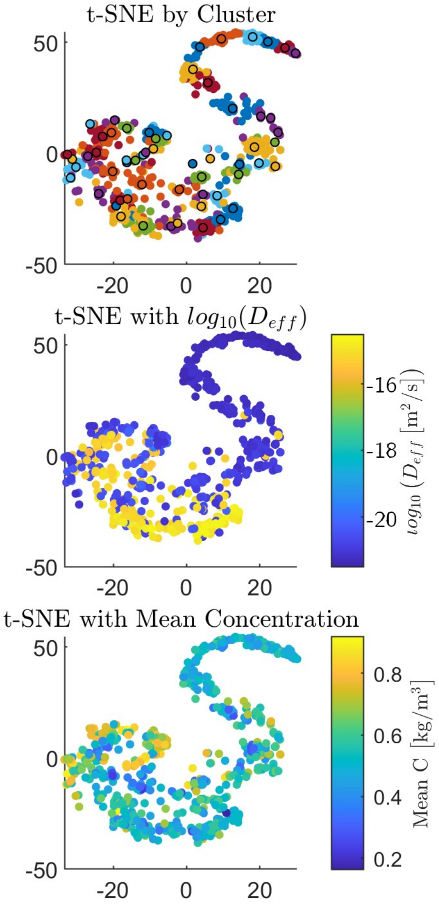

Figure 15: t-SNE embedding colored by Cluster, D_{eff}, and mean concentration respectively. Note the inverse relation between D_{eff} and concentration at (-10,0).

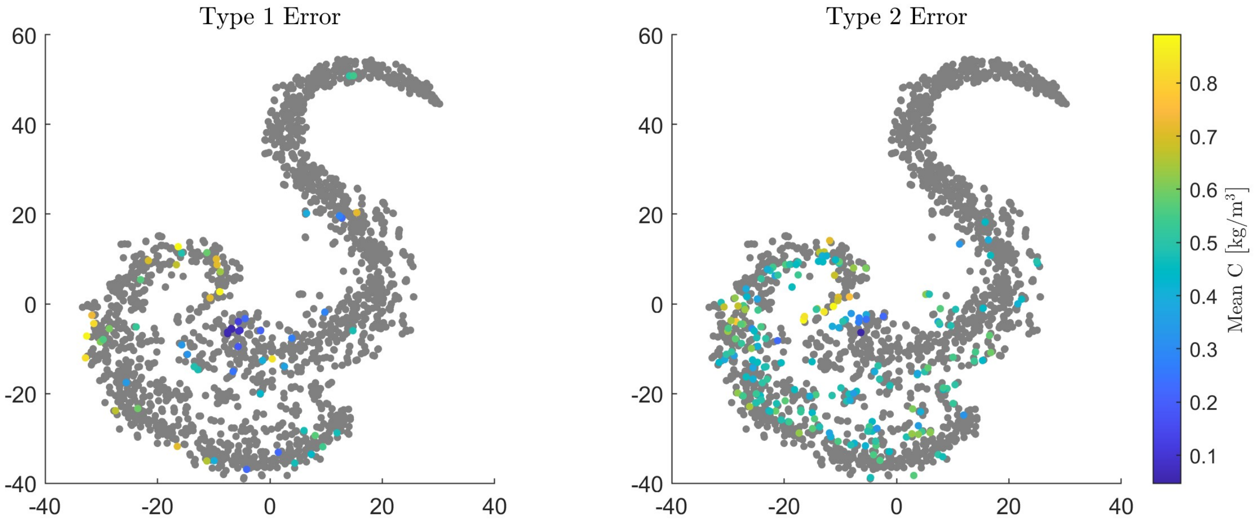

Figure 16: Type 1 and type 2 errors found from p_c, embedded into t-SNE. Note the local correlations with mean C.

GBN with a single boundary type, the expected concentration behavior would be a linear gradient across the microstructure from source to sink. With our stated boundary conditions, C_n would have an average value of about $0.5\,\mathrm{kg/m^3}$.

Coloring the markers by mean concentration on the t-SNE embedding (Fig. 15), we can see that the areas correlating with the J_3 and J_0 corners (the homogeneous single boundary type regions) exhibit a mean C_n of $0.5\,\mathrm{kg/m^3}$, as expected. However, there are microstructures with significantly higher or lower average concentration, especially in the previously mentioned J_1 region. Since the exceptions are well localized in the t-SNE embedding, and the embedding uses the power spectrum and not C_n, the power spectra enable the interpretation of the non-average behavior.

From Eq. 14 we have the direct link (A) between structure (U) and performance (C_n). To interpret this, remember that the sign of all u_k was chosen to ensure that $a_k \geq 0 \,\forall\, k$. Therefore, a positive value in u_k represents a positive concentration contribution of magnitude $a_k \cdot u_k$ for each vertex n.

From our results in Section 3.2, we know that eigenvectors highlight connected sections of boundaries of a given type and we expect a steady gradient from source to sink. Therefore, if the concentration average is skewed, and the eigenvector contributions are strictly additive, then the deviation of mean C_n from $0.5\,\mathrm{kg/m^3}$ is caused by a connected set of boundaries of a given type that do not connect the source and sink.

We show a specific example of this in Fig. 17, where we take 3 microstructures that all have identical TJFs and similar D_{eff}, but very different C_n and power spectra. Fig. 17 shows the power spectrum of each microstructure, as well as the mean concentration colored t-SNE coordintates and C_n responses for each.

This allows us to illustrate an interesting link between the microstructure and the power spectrum, where Struct 3 only has a single, small amplitude, peak above the spectral gap, despite having an identical TJF and comparable connectivity to the other two microstructures. This signature in the power spectrum is indicative of the HAGB

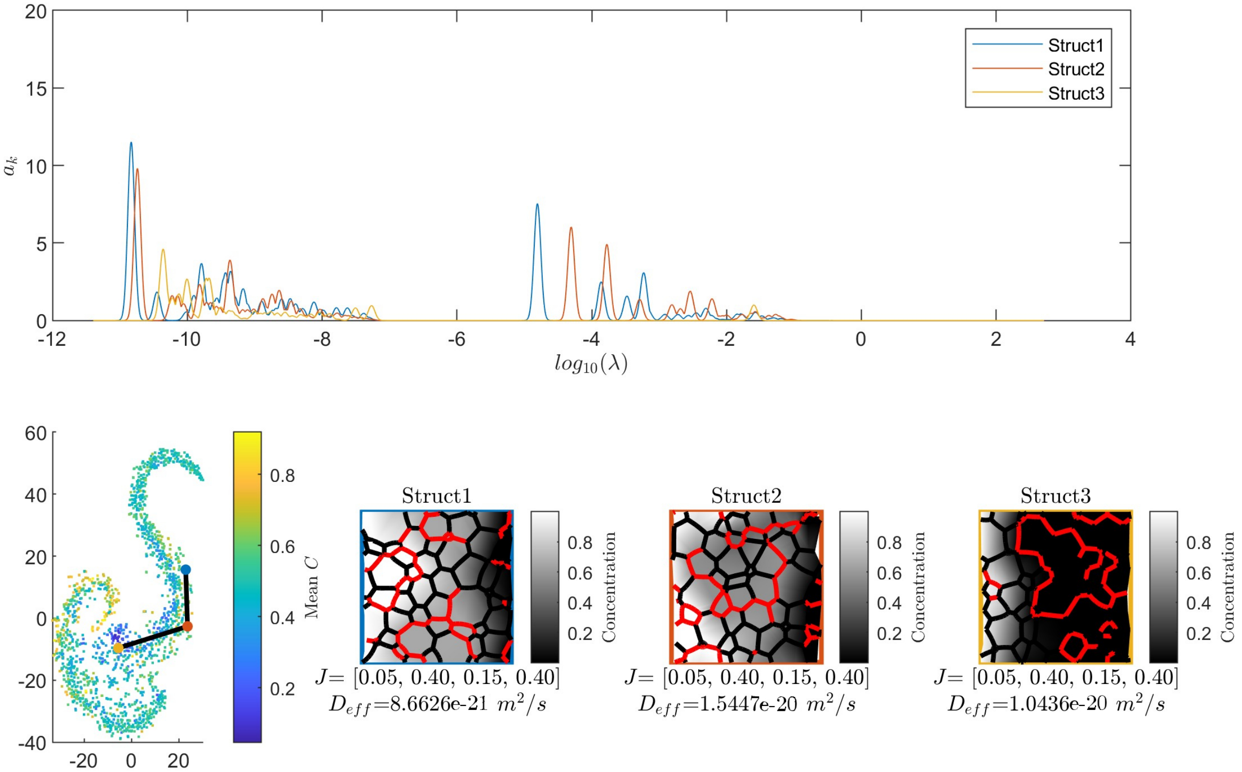

Figure 17: An example of three microstructures with identical TJF, similar D_{eff}, but different C_n and power spectra behavior. The three structure markers in t-SNE (bottom-left) are colored the same as their respective power spectra (top).

cluster being connected only to the diffusion *sink* and implies that the HAGBs do not contribute significantly to C_n, leading to a sharp concentration gradient near the diffusion source that stops at the highly connected HAGB section, resulting in a low value of mean C_n (since most vertices have nearly the same concentration as the sink). This explains one of the false-positives identified earlier (percolation is predicted from the short-range correlations encoded in the J_i, but is not actually observed due to long-range effects).

A similar behavior occurs when a highly connected, but non-percolating, HAGB section is connected to the diffusion *source*, where instead the concentration is very high throughout the concentration profile (most vertices have essentially the same concentration as the source).

Speaking more generally, the power spectrum clustering distinguished these disconnected features, shown in Fig. 15, with the high and low mean C_n groupings in t-SNE. When considering mean C_n greater than $0.8\,\mathrm{kg/m^3}$ or less than $0.2\,\mathrm{kg\,m^{-1}}$, we find that 20 of the 61 type 1 errors exhibit the sharp concentration gradient behavior.

Plotting the power spectra of all clusters enables the identification of connected boundaries that are disconnected from the source and sink, as shown in Fig. 18. The general trend is that microstructures with low D_{eff} are dominated by low frequency eigenmodes, and GBNs that exhibit high D_{eff} are dominated by high frequency eigenmodes. However, there are many low frequency dominated clusters that also have significant contributions from high frequency eigenmodes. Interpreting such signatures in the context of the results just discussed suggests that these microstructures have highly interconnected HAGBs that are well connected with the diffusion source, but do not percolate.

Understanding the type 2 errors is more difficult, as the only way to currently understand the configurational differences that cause a microstructure to percolate unexpectedly is by directly investigating individual dominant eigenvectors for each microstructure. Future work could focus on finding

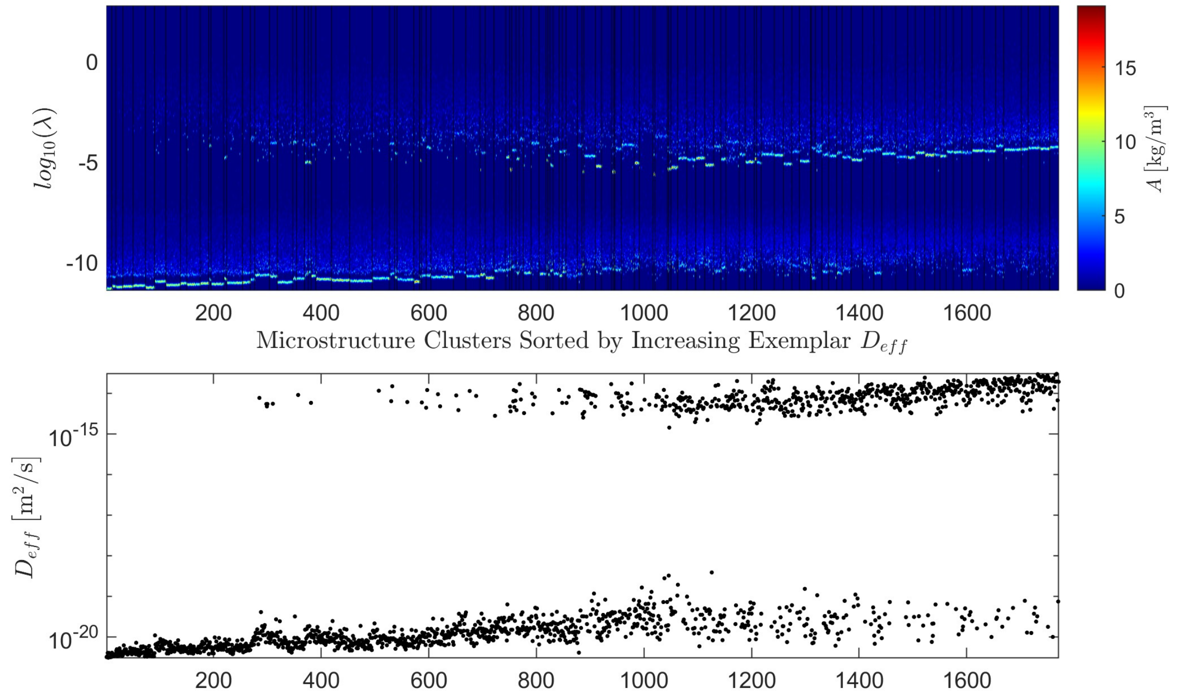

Figure 18: Power spectra of all microstructures, sorted according to cluster first and D_{eff} of exemplars second. Note the general trend of transitioning from dominant low frequency peaks to dominant high frequency peaks as D_{eff} of the cluster exemplar increases.

and automating the identification and classification of specific eigenvectors, which would allow for analysis of these specific cases.

4.3. Applications to Experimental Data

While we have focused a majority of this work on simulated microstructures, this methodology can be applied to experimentally obtained samples. To illustrate this, we will apply the methods of the present work to an experimental dataset from Randle et al [25, 26].

This dataset contains nickel samples in a reference state and a grain boundary engineered (GBE) state, where at least 50% of all grain boundaries were $\Sigma 3$. We make the same assumptions from Section 2.1 while applying our method to these microstructures, and used MTEX and grain reconstruction code to generate the GBN meshes from the available grain boundary segment data [27–30].

As $\Sigma 3$ GBs have unique properties and there is a large population of them in this dataset, we adapt our hypothetical constitutive model accordingly. Specifically, following the logic of previous diffusion work on FCC polycrystals, we consider both $\Sigma 3$ GBs and LAGBs ($<15^\circ$ disorientation) as "special" boundaries and therefore assign them both the same low diffusivity as before. We note that this assumption does not hold for all systems [19, 32–34]. Additionally, since these microstructures are non-periodic we set the upper and lower borders to have Neumann boundary conditions, which, conveniently, does not change the derived calculations in Section 2.1.

An example comparison is shown in Fig. 19 for a reference state and engineered nickel sample. The increased proportion of $\Sigma 3$ boundaries is visible both spatially in the GBN map and spectrally from the increased low eigenvalue peak (and diminished high eigenvalue peak) in the power spectrum of the GBE sample. More interestingly, the most dominant eigenvector shows how the increased proportion of $\Sigma 3$ boundaries interrupts the connectiv-

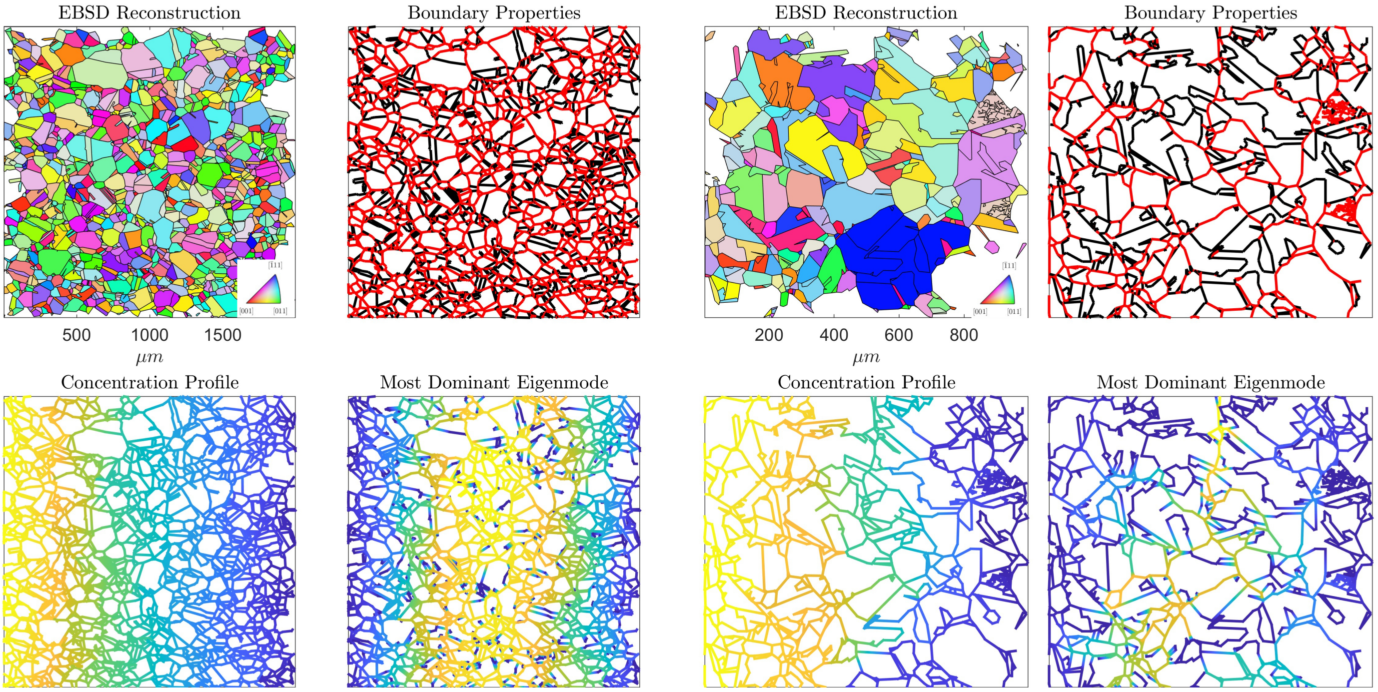

(a) Reference state Ni sample

(b) Grain boundary engineered Ni sample

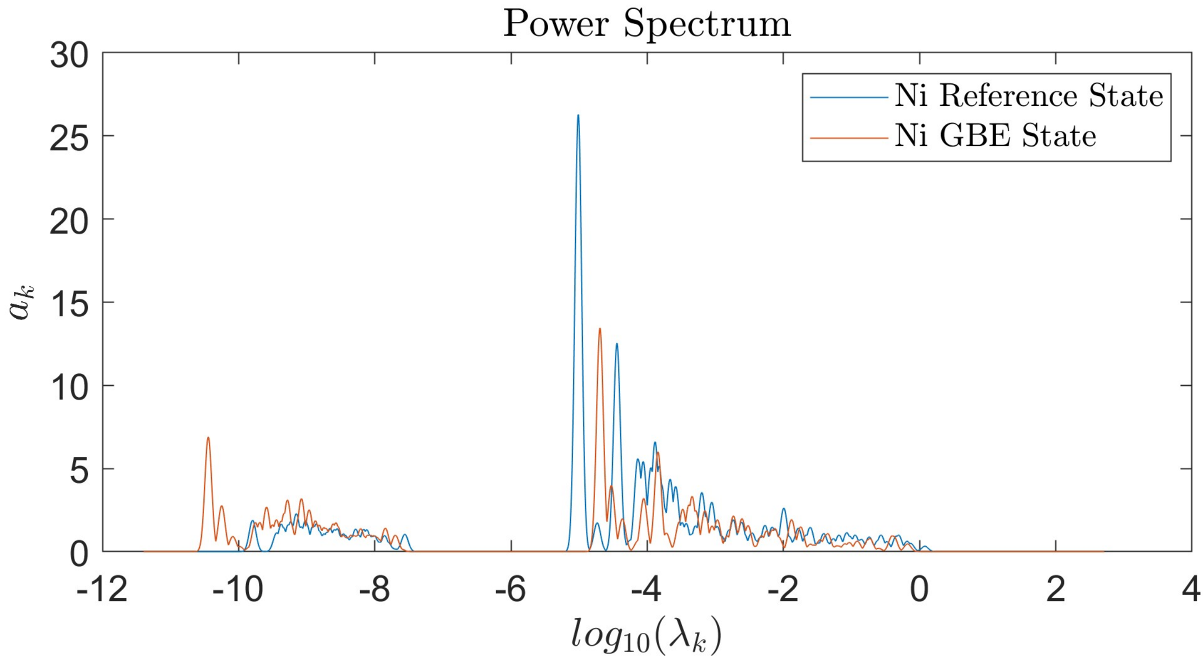

(c) Power Spectra of both structures

Figure 19: Example of the methods applied to analysis of grain boundary engineered sample against a reference sample. Note that the engineered sample is still dominated by high diffusivity boundaries, but has much less connectivity than the reference sample. In the IPF maps, the perimeter grains are not colored because some perimeter edges were not included in the dataset so that these are not closed regions. This, however, only affects the visualization and has no impact for the purposes of the present analysis.

ity of high angle boundaries, resulting in a more spatially sparse dominant eigenvector for the engineered sample.

However, even with the grain boundary engineering we can see that the high-angle boundaries are still dominant in the diffusion equation, meaning

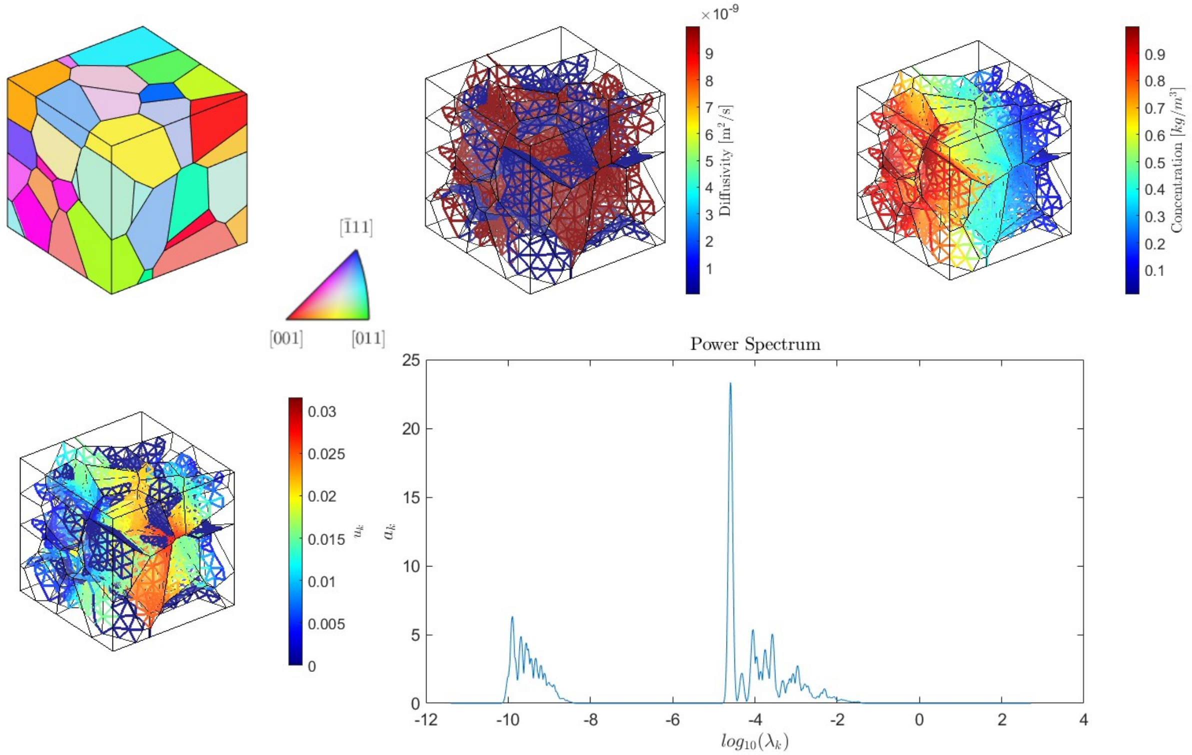

Figure 20: Example of applying the power spectra methodology to 3D microstructures according to the model presented in previous work [31]. The most dominant eigenvector is shown. Note the changing concentrations and eigenvectors along grain boundary planes.

that in order to affect diffusion in this model more strongly a sample would need greater fractions of connected Σ3 or low angle boundaries than are currently present.

4.4. Extension to 3D

Previous work by the authors extended the kinetic type-C regime diffusivity model to 3D microstructures using a finite volume method, which provides a simple extension to the current work [31]. We simulate and mesh a 1 cm^3 grain growth morphology microstructure using Neper Polycrystal for this example [35].

We use the same boundary conditions as the previous work, with Dirichlet conditions in the X-direction, using the same values as in Section 2.1, and Neumann in all other directions [31]. This means that the boundary conditions are applied to a plane, rather than a line (as in the 2D case).

However, once these conditions are set and properties have been assigned to each boundary, there are no additional changes needed to the methods to achieve the power spectra or eigenvector embeddings. This simple extension is shown in Fig. 20 for the example 3D microstructure. Thus, the same tools can be employed to analyze 3D microstructures.

Further extensions can be made to this model in similar ways, as long as a graph representation is defined and maintained through the derivation. Model additions such as bulk transport or triple line specific effects can be derived and analyzed using the same methodology. This would require an understanding of, and model values for, the bulk diffusivity and TJ specific diffusivity to apply to the graph edges, as well as expanding the finite volume method of the 3D model to account for tetrahedral elements. Even more general, other property equations follow a similar harmonic form, such as the heat equation, and can be derived in a way that allows the current analysis to be done for other GBN structure property models [36].

5. Conclusions

Since there are situations where microstructures can have identical local structural measures, yet large property differences due to long range grain boundary network (GBN) effects, we created a method for encoding, comparing, and interpreting complete GBN connectivity and structural information through a harmonic representation. This representation encodes both compositional and long-range configurational information into a descriptor: the GBN power spectrum.

Here we summarize the insights gleaned and capabilities demonstrated by application of the GBN power spectrum to the problem of intergranular diffusion:

- We showed how microstructures can be compared, even with different morphologies, boundary configurations and discretizations, via the power spectrum descriptor.
- We showed how this descriptor enables identification of network length effects that cause property differences that classical GBN descriptors (TJF and p) could not. We provided a physical interpretation of the eigenmodes of the power spectrum, identifying structural features that influence effective properties.
- We applied this descriptor to a large library of microstructures, and found multiple classes of structural similarities through clustering.
- We compared and interpreted these clusters in the context of our GBN power spectrum descriptor and the classical descriptors, finding that microstructures with either equal proportions of TJ boundary types or with high J_1 populations have properties that are very sensitive to perturbations of boundary configurations, while microstructures with high J_2-J_3 populations are very stable against the similar perturbations.
- We also found conditions where the current descriptor can identify and explain unexpected percolation or lack of percolation in microstructures, compared to predictions based on local correlations alone.
- We showed examples of how this method and analysis can be applied to experimental and 3D microstructures.

We anticipate that the GBN power spectrum approach may enable characterization of GBNs and their impact on performance, both for diffusion and more generally. Extension to other properties of interest (e.g., heat transfer or fracture) may be accomplished by selection of appropriate weights in the GBN Laplacian.

Acknowledgement

The material presented here is based upon work supported by the National Science Foundation under Grant No. DMR-1654700.

Declaration of Interest

The authors declare that they have no known competing financial interests or personal relationships that could have appeared to influence the work reported in this paper.

Appendix A Sensitivity Analysis of Distance Measure

To select the standard deviation of the Gaussian we performed the calculation from Eq. 15 for all 1771 microstructures for each σ in the range of $[0.001, .1]$ incrementing by 0.001 length steps. We calculated an estimated gradient of Eq. 15 as the first order difference over σ to test for stability of Eq. 15 vs σ.

The results of these two operations can be seen in Fig. 21, where each line is a single microstructure, the top tile is the distance vs σ, and the bottom tile is the derivative estimate of the top tile. To avoid losing information by oversmoothing we select the smallest σ possible that ensures that the calculated distances, $d(A_i, A_j)$, are stable against perturbations of sigma. We find $\sigma = 0.05$ to be the smallest value of σ where the gradient is at a locally stable value.

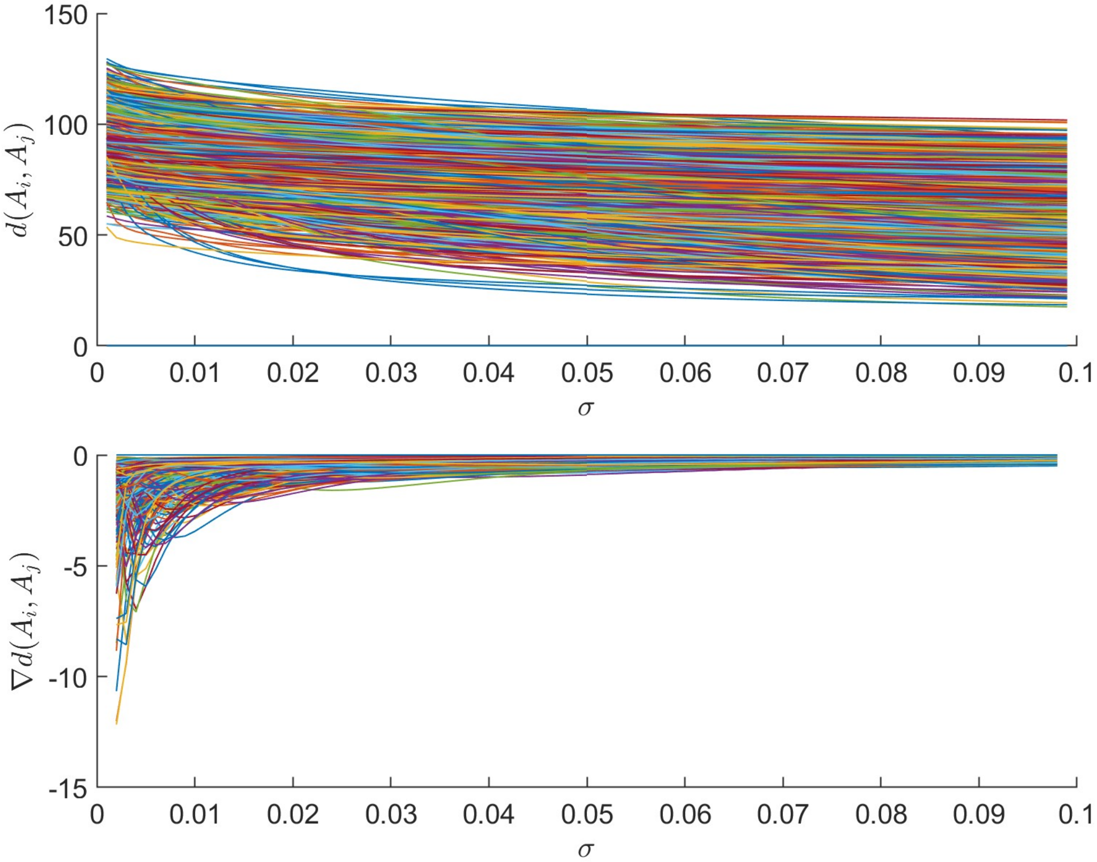

Figure 21: Sensitivity analysis of $d(A_i, A_j)$ vs σ for all microstructures. The goal was to select a σ as small as possible that would also ensure $d(A_i, A_j)$ would be stable against small perturbations of σ.

References

[1] O. K. Johnson, J. M. Lund, T. R. Critchfield, Spectral graph theory for characterization and homogenization of grain boundary networks, Acta Materialia 146 (2018) 42–54. doi:10.1016/j.actamat.2017.11.054.

[2] B. D. Snow, S. G. Baird, C. Kurniawan, D. T. Fullwood, E. R. Homer, O. K. Johnson, Grain boundary structure-property model inference using polycrystals: The underdetermined case, Acta Materialia 209 (2021) 116769. URL: https://doi.org/10.1016/j.actamat.2021.116769. doi:10.1016/j.actamat.2021.116769.

[3] S. G. Baird, E. R. Homer, D. T. Fullwood, O. K. Johnson, Five degree-of-freedom property interpolation of arbitrary grain boundaries via Voronoi fundamental zone framework, Computational Materials Science 200 (2021) 110756. URL: https://doi.org/10.1016/j.commatsci.2021.110756. doi:10.1016/j.commatsci.2021.110756.

[4] B. B. Zhang, Y. G. Tang, Q. S. Mei, X. Y. Li, K. Lu, Inhibiting creep in nanograined alloys with stable grain boundary networks, Science 378 (2022) 659–663. doi:10.1126/science.abq7739.

[5] W. Feng, Z. Wang, Q. Sun, Y. He, Y. Sun, Effect of thermomechanical processing via rotary swaging on grain boundary character distribution and intergranular corrosion in 304 austenitic stainless steel, Journal of Materials Research and Technology 19

(2022) 2470–2482. URL: https://doi.org/10.1016/j.jmrt.2022.06.032. doi:10.1016/j.jmrt.2022.06.032.

[6] D. jun Liu, G. Tian, G. feng Jin, W. Zhang, Y. hong Zhang, Characterization of localized corrosion pathways in 2195-T8 Al–Li alloys exposed to acidic solution, Defence Technology 25 (2023) 152–165. URL: http://dx.doi.org/10.1016/j.dt.2022.05.004. doi:10.1016/j.dt.2022.05.004.

[7] S. Patala, J. K. Mason, C. A. Schuh, Improved representations of misorientation information for grain boundary science and engineering, Progress in Materials Science 57 (2012) 1383–1425. URL: http://dx.doi.org/10.1016/j.pmatsci.2012.04.002. doi:10.1016/j.pmatsci.2012.04.002.

[8] J. Guo, Q. Lou, Y. Qiu, Z. Y. Wang, Z. H. Ge, J. Feng, J. He, Remarkably enhanced thermoelectric properties of Bi2S3 nanocomposites via modulation doping and grain boundary engineering, Applied Surface Science 520 (2020) 146341. URL: https://doi.org/10.1016/j.apsusc.2020.146341. doi:10.1016/j.apsusc.2020.146341.

[9] M. Shimada, H. Kokawa, Z. Wang, Y. Sato, I. Karibe, Optimization of grain boundary character distribution for intergranular corrosion resistant 304 stainless steel by twin-induced grain boundary engineering, Acta Materialia 50 (2002) 2331–2341. URL: http://linkinghub.elsevier.com/retrieve/pii/S1359645402000642. doi:10.1016/S1359-6454(02)00064-2.

[10] S. Fu, Y. Arinicheva, C. Hüter, M. Finsterbusch, R. Spatschek, Grain Boundary Characterization and Potential Percolation of the Solid Electrolyte LLZO, Batteries 9 (2023) 1–14. doi:10.3390/batteries9040222.

[11] M. E. Frary, C. A. Schuh, Correlation-space description of the percolation transition in composite microstructures, Physical Review E - Statistical, Nonlinear, and Soft Matter Physics 76 (2007). doi:10.1103/PhysRevE.76.041108.

[12] V. C. Moreira, A. P. Tschiptschin, J. C. Dutra, Improvements on the characterization of heterogeneities in grain size by network analysis, Materials Characterization 195 (2023). doi:10.1016/j.matchar.2022.112551.

[13] L. G. Harrison, Influence of dislocations on diffusion kinetics in solids with particular reference to the alkali halides, Transactions of the Faraday Society 57 (1961). doi:10.1039/TF9615701191.

[14] V. Tcherdyntsev, A. Rodin, The Algorithm to Predict the Grain Boundary Diffusion in Non-Dilute Metallic Systems, Materials 16 (2023). doi:10.3390/ma16041431.

[15] S. Butler, F. Chung, Spectral Graph Theory, in: Handbook of Linear Algebra, Second Edition, 2013. doi:10.1017/cbo9780511529993.006.

[16] L. J. Grady, J. R. Polimeni, Discrete calculus: Applied analysis on graphs for computational science, 2010. doi:10.1007/978-1-84996-290-2.

[17] C. A. Schuh, M. Kumar, W. E. King, Analysis of grain boundary networks and their evolution during grain boundary engineering, Acta Materialia 51 (2003) 687–700. URL: http://www.sciencedirect.com/science/article/pii/S1359645402004470. doi:10.1016/S1359-6454(02)00447-0.

[18] J. Sayet, B. O. Hoch, A. Oudriss, J. Bouhattate, X. Feaugas, Multi-scale approach to hydrogen diffusion in FCC polycrystalline structure with binary classification of grain boundaries in continuum model, Materials Today Communications 34 (2023) 105021. URL: https://doi.org/10.1016/j.mtcomm.2022.105021. doi:10.1016/j.mtcomm.2022.105021.

[19] A. Oudriss, J. Creus, J. Bouhattate, E. Conforto, C. Berziou, C. Savall, X. Feaugas, Grain size and grain-boundary effects on diffusion and trapping of hydrogen in pure nickel, Acta Materialia 60 (2012) 6814–6828. URL: http://dx.doi.org/10.1016/j.actamat.2012.09.004. doi:10.1016/j.actamat.2012.09.004.

[20] T. Needham, The Geometry of Harmonic Functions, Mathematics Magazine 67 (1994). doi:10.2307/2690683.

[21] W. Jiang, A. Wieczorkowska, Z. W. Raś, Music instrument estimation in polyphonic sound based on short-term spectrum match, Studies in Computational Intelligence 202 (2009). doi:10.1007/978-3-642-01533-5_10.

[22] Y. Gonzalez, R. C. Prati, Acoustic Descriptors for Characterization of Musical Timbre Using the Fast Fourier Transform, Electronics (Switzerland) 11 (2022). doi:10.3390/electronics11091405.

[23] F. Bavaud, Euclidean distances, soft and spectral clustering on weighted graphs, in: Lecture Notes in Computer Science (including subseries Lecture Notes in Artificial Intelligence and Lecture Notes in Bioinformatics), volume 6321 LNAI, 2010. doi:10.1007/978-3-642-15880-3_13.

[24] B. J. Frey, D. Dueck, Clustering by passing messages between data points, Science 315 (2007). doi:10.1126/science.1136800.

[25] V. Randle, G. S. Rohrer, H. M. Miller, M. Coleman, G. T. Owen, Five-parameter grain boundary distribution of commercially grain boundary engineered nickel and copper, Acta Materialia 56 (2008) 2363–2373. doi:10.1016/j.actamat.2008.01.039.

[26] G. S. Rohrer, The Grain Boundary Data Archive, 2023. URL: http://mimp.materials.cmu.edu/$\sim$gr20/Grain_Boundary_Data_Archive/.

[27] R. Krakow, R. J. Bennett, D. N. Johnstone, Z. Vukmanovic, W. Solano-Alvarez, S. J. Lainé, J. F. Einsle, P. A. Midgley, C. M. Rae, R. Hielscher, On three-dimensional misorientation spaces, Proceedings of the Royal Society A: Mathematical, Physical and Engineering Sciences 473 (2017). doi:10.1098/rspa.2017.0274.

[28] R. Hielscher, T. Nyyssönen, F. Niessen, A. A. Gazder, The variant graph approach to improved parent grain reconstruction, Materialia 22 (2022) 101399. URL: https://doi.org/10.1016/j.mtla.2022.101399. doi:10.1016/j.mtla.2022.101399. arXiv:2201.02103.

[29] Jos, PADCAT, 2024. URL: https://www.mathworks.com/matlabcentral/fileexchange/22909-padcat.

[30] M. J, spatialgraph2D, 2024. URL: https://www.mathworks.com/matlabcentral/fileexchange/73630-spatialgraph2d.

[31] C. W. Adair, H. Evans, E. Beatty, D. L. Hansen, S. Holladay, O. K. Johnson, Microstructure design using a human computation game, Materialia 25 (2022) 101544. URL: https://doi.org/10.1016/j.mtla.2022.101544. doi:10.1016/j.mtla.2022.101544.

[32] S. Hao, H. Li, Effect of twin grain boundary on the diffusion of Cu in bulk β-Sn, Computational Materials Science 226 (2023) 112200. URL: https://doi.org/10.1016/j.commatsci.2023.112200. doi:10.1016/j.commatsci.2023.112200.

[33] T. Luo, Y. Peng, Y. Guo, J. Cao, Influence of interactions between hydrogen and (101¯2) twin boundary on hydrogen embrittlement in α-Ti, Materials Today Communications 26 (2021) 101802. URL: https://doi.org/10.1016/j.mtcomm.2020.101802. doi:10.1016/j.mtcomm.2020.101802.

[34] R. Wang, X. Chen, Z. Huang, J. Yang, F. Liu, M. Chu, T. Liu, C. Wang, W. Zhu,

S. Li, S. Li, J. Zheng, J. Chen, L. He, L. Jin, F. Pan, Y. Xiao, Twin boundary defect engineering improves lithium-ion diffusion for fast-charging spinel cathode materials, Nature Communications 12 (2021) 1–10. URL: http://dx.doi.org/10.1038/s41467-021-23375-7. doi:10.1038/s41467-021-23375-7.

[35] R. Quey, P. R. Dawson, F. Barbe, Large-scale 3D random polycrystals for the finite element method: Generation, meshing and remeshing, Computer Methods in Applied Mechanics and Engineering 200 (2011) 1729–1745. URL: http://dx.doi.org/10.1016/j.cma.2011.01.002. doi:10.1016/j.cma.2011.01.002.

[36] K. Saito, A. Dhar, Generating function formula of heat transfer in harmonic networks, Physical Review E - Statistical, Nonlinear, and Soft Matter Physics 83 (2011) 1–4. doi:10.1103/PhysRevE.83.041121. arXiv:1012.0622.